

ORIGINAL RESEARCH ARTICLE

Influence of laser power and hatch spacing
on the mechanical properties of AlSi10Mg
processed by selective laser meltingXabier Sandua^{1,2} , Eneko Arbizu¹ , Álvaro Rodríguez^{1,3}, Fernando Veiga^{1*} ,
Miguel Ángel Martín^{1,2} , and Pedro J. Rivero^{1,2} ¹Department of Engineering, Public University of Navarra, Campus Arrosadía, 31006 Pamplona, Navarra, Spain²Institute for Advanced Materials and Mathematics (INAMAT2), Public University of Navarra, Campus Arrosadía, 31006 Pamplona, Navarra, Spain³Department of Transportation and Maintenance of Vehicles, CIFP Fontecarmoa, 36600 Vilagarcía de Arousa, Pontevedra, Spain

Abstract

Selective laser melting (SLM) of AlSi10Mg is widely used for lightweight engineering applications, but the combined effects of key process parameters on densification, microstructure, and mechanical performance remain incompletely understood. This study systematically investigated the combined effects of laser power (200–230 W) and hatch spacing (0.11–0.15 mm) on the densification, mechanical behavior, and microstructural characteristics of AlSi10Mg components fabricated by SLM. A statistically rigorous approach based on two-way ANOVA and ordinary least squares regression was employed to quantify the individual and interactive influence of process parameters on relative density, surface porosity, hardness, Charpy impact energy, and tensile properties. The results show that laser power is the dominant parameter affecting densification and impact energy, whereas hatch spacing exhibits no statistically significant influence within the investigated range. Maximum relative densities above 99.7% were achieved at low laser powers (200–210 W), while hardness increased with increasing power, reaching approximately 140 HV at 230 W. The highest impact energy was obtained at an intermediate laser power of 210 W, indicating a favorable intermediate energy input under the tested conditions. Tensile testing revealed that the highest ultimate tensile strength was achieved at 220 W with a hatch spacing of 0.15 mm, despite slightly lower density and hardness values compared to other samples. Microstructural and fractographic analyses demonstrate that tensile performance is strongly governed by solidification morphology and defect distribution rather than density alone. This systematic, statistically supported evaluation advances the understanding of process–property relationships in SLM AlSi10Mg and provides practical guidance for parameter optimization in engineering applications.

Keywords: Selective laser melting; AlSi10Mg; Laser power; Hatch spacing***Corresponding author:**Fernando Veiga
(fernando.veiga@unavarra.es)

Citation: Sandua X, Arbizu E, Rodríguez A, Veiga F, Martín MA, Rivero PJ. Influence of laser power and hatch spacing on the mechanical properties of AlSi10Mg processed by selective laser melting. *Mater Sci Add Manuf*. 2026;5(2):026040008.
doi: 10.36922/MSAM026040008

Received: January 24, 2026**Revised:** February 17, 2026**Accepted:** March 3, 2026**Published online:** May 18, 2026

Copyright: © 2026 Author(s). This is an Open-Access article distributed under the terms of the Creative Commons Attribution License, permitting distribution, and reproduction in any medium, provided the original work is properly cited.

Publisher's Note: AccScience Publishing remains neutral with regard to jurisdictional claims in published maps and institutional affiliations.

1. Introduction

Additive manufacturing (AM), commonly known as three-dimensional (3D) printing, refers to a collection of technologies that create three-dimensional objects by sequentially depositing material layer by layer, guided by digital models.¹ Unlike traditional subtractive manufacturing methods, which shape parts by removing material from a solid block, AM offers significant advantages, such as reduced material waste, shortened production cycles, and the ability to fabricate complex geometries that would be difficult or impossible to achieve using conventional techniques. These capabilities have positioned AM as a transformative technology across various sectors, including aerospace, automotive, medical, and consumer goods.²

Among the various AM technologies, metal AM techniques have received growing interest due to their ability to produce high-performance components directly from metal powders. One of the most prominent methods in this category is selective laser melting (SLM), a powder bed fusion process that uses a high-power laser to selectively melt and consolidate metal powder particles layer by layer. The resulting parts can achieve high densities, excellent mechanical properties, and high geometric accuracy, making SLM a suitable technology for the production of functional and structural metal parts.³ SLM offers several notable benefits: it eliminates the need for traditional tooling, reduces lead times, and allows for the integration of complex internal features within a single component. Consequently, it has become a preferred method for producing customized, lightweight, and high-strength components in industries with stringent performance requirements.⁴ The effectiveness of the SLM process, however, is highly sensitive to a range of process parameters, such as laser power, scanning speed, layer thickness, and hatch spacing. These parameters directly affect the energy input during the melting process, which in turn influences powder consolidation, melt pool stability, porosity formation, residual stresses, and mechanical properties of the final part.⁵

Among the materials processed by SLM, AlSi10Mg has emerged as one of the most widely used due to its excellent weldability, low density, good thermal conductivity, and well-balanced mechanical properties.⁶ These characteristics make AlSi10Mg particularly attractive for applications requiring lightweight and thermally stable components, such as in the automotive and aerospace industries⁷. To fully understand the influence of processing parameters on the final part performance, it is essential to conduct detailed microstructural and fractographic analyses. These analyses provide insight into failure mechanisms

and allow correlation between process conditions and material behavior beyond standard mechanical tests.⁸ Extensive research has been conducted to investigate how SLM process parameters affect the microstructure and mechanical performance of AlSi10Mg components.^{6,9} Campanelli *et al.*¹⁰ reviewed how different laser powers and scan strategies directly influence the resultant porosity levels, microstructural evolution, and tensile properties. Tolosa *et al.*¹¹ compared SLM-processed AlSi10Mg to cast counterparts and observed significantly improved tensile strength and hardness, which was attributed to rapid solidification and fine microstructural features. Similarly, studies on stainless steel and other alloys have shown that both laser power and hatch spacing critically influence melt pool behavior and final part integrity.¹²

Previous studies have shown that AlSi10Mg components produced by SLM can achieve mechanical properties comparable to, or even exceeding, those of conventionally cast alloys. In particular, Kempen *et al.*¹³ attributed this behavior to the refined microstructure and homogeneous silicon distribution characteristic of the SLM process, while also reporting anisotropy in ductility associated with process-induced porosity and scanning strategy. More recent investigations, such as the work by Roth *et al.*¹⁴, confirmed the superior strength and lower porosity of SLM-manufactured AlSi10Mg compared to cast material, but additionally revealed a pronounced dependence of the mechanical response on build height and stress state. These findings emphasize the need for a deeper understanding of how SLM process parameters govern microstructure–property relationships. In contrast, Snopiński *et al.*¹⁵ explored post-processing approaches to address the limited ductility and yield strength of SLM-produced AlSi10Mg, demonstrating that severe plastic deformation techniques such as equal-channel angular pressing can effectively reduce porosity and refine the grain structure, leading to significant hardness improvements; however, such enhancements rely on additional processing steps rather than direct optimization of the SLM process itself.

Despite the substantial body of work on AlSi10Mg, considerable variation still exists in the reported results across different machines, settings, and experimental conditions. This variability underscores the importance of systematic studies that isolate the effects of key process parameters to develop robust, generalizable guidelines for process optimization. Furthermore, many existing studies focus either on isolated parameters or on proprietary, machine-specific configurations, limiting their applicability to broader industrial contexts.¹⁶

Although optimization of laser powder bed fusion

(LPBF) process parameters can significantly improve densification and mechanical properties, some inherent limitations, such as microstructural heterogeneity, residual stresses, and mechanical anisotropy, cannot be fully resolved through parameter adjustment alone. For this reason, complementary approaches such as thermal post-processing have been widely investigated. Treatments including annealing, solution heat treatment, and T6 aging have been shown to enhance microstructural homogeneity and improve hardness distribution in AlSi10Mg components.¹⁷ Furthermore, comprehensive reviews have highlighted that, despite the significant progress achieved in LPBF of aluminium alloys, challenges related to defect formation, process stability, and microstructure–property relationships still limit full industrial implementation, underscoring the need for a deeper understanding of both process optimization and post-processing strategies.¹⁸

In this study, a systematic experimental investigation was conducted to address the existing gap in understanding the combined effects of laser power and hatch spacing on the mechanical and microstructural performance of SLM-processed AlSi10Mg. While numerous studies have examined individual process parameters or optimized machine-specific settings, there remains a lack of statistically supported analyses that isolate and compare the relative importance of these two key energy-related parameters across multiple mechanical responses. Here, laser power and hatch spacing were varied within controlled ranges to evaluate their influence on relative density, surface porosity, hardness, impact toughness, and tensile behavior. The novelty of this work lies in the simultaneous assessment of these parameters using both mechanical testing and microstructural and fractographic analyses, supported by two-way analysis of variance (ANOVA) and

regression models to quantify parameter significance. Furthermore, this study demonstrates that optimal tensile performance does not necessarily correspond to maximum density or hardness, highlighting the critical role of solidification morphology and defect distribution. The findings contribute generalizable insights into process–property relationships and provide practical guidelines for balancing energy input, mechanical performance, and defect control in industrial SLM applications of AlSi10Mg.

2. Materials and methods

This section describes the fabrication equipment, process parameters, and materials employed in this study.

2.1. Experimental set-up

The specimens were manufactured using an Alba 300 SLM machine developed by SamyLabs (Spain). This equipment is specifically designed for industrial and research applications in metals and allows precise adjustment of critical parameters such as laser power, hatch spacing, scanning speed, and bed temperature. The Alba 300 is equipped with a 300 W fiber laser and operates in a controlled inert gas atmosphere (argon), ensuring stable conditions during the melting process and minimizing oxidation of the metal powder. Its versatility and reliability make it a suitable tool for experimental studies such as this one, where precise control of processing conditions is required. [Figure 1](#) shows the schematic representation of the employed SLM equipment. The specimens were fabricated as truncated inverted pyramids ($15 \times 15 \times 10$ mm) under selected combinations of laser power and hatch spacing used in this study, and were then analyzed for density, surface porosity, hardness, and microstructural characteristics ([Figure 2](#)). Argon was used as the shielding gas, with chamber oxygen levels below 1,000 ppm. The

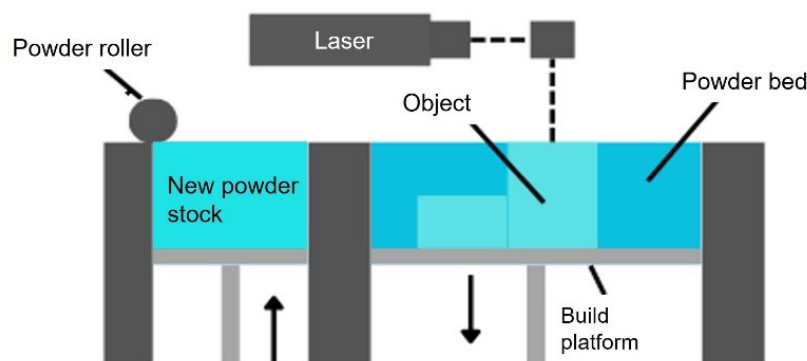


Figure 1. Schematic representation of the selective laser melting process employed in this study

laser spot size was less than 100 μm , with a wavelength of 1,080 nm, and the build chamber dimensions were 730 \times 1,550 \times 1,850 mm. The arrangement of specimens in the chamber and their corresponding powers and hatch spacings are shown in [Figure 2A](#).

The material used in this study was AlSi10Mg metal powder (from m4p, Germany), an aluminum alloy with approximately 10% silicon and small amounts of magnesium ([Table 1](#)), specifically designed for additive manufacturing processes using laser melting. The powder exhibits a predominantly spherical morphology, suitable for accurate dosing and homogeneous distribution across the build platform.¹⁹

The powder was supplied in the $-63/+20$ μm size fraction, corresponding to the sieve-classified range recommended by the manufacturer for LPBF applications. According to the manufacturer's datasheet, the powder exhibits predominantly spherical morphology, characteristic of gas-atomized particles, ensuring suitable flowability and packing behavior for powder bed fusion applications. The theoretical density of the material is 2.7 g/cm³, which is used as a reference to calculate the relative density of the fabricated parts. This alloy is widely used due to its good mechanical strength, light weight, and corrosion resistance, making it common in sectors such as automotive, aerospace, and the production of structural tooling.¹⁹

2.2. Process parameters

During the fabrication of the specimens, several process parameters were kept constant in order to isolate the effect of the variables under study. The scanning speed was set at 800 mm/s, and the layer thickness at 25 μm . Laser powers ranging from 180 W to 300 W were examined in preliminary trials; based on those results, 200 W, 210 W, 220 W, and 230 W were selected for the presented study.

In combination, hatch spacing values ranging from 0.11 mm to 0.15 mm were also evaluated. These two parameters were chosen due to their direct influence on the volumetric energy input, and consequently on interlayer bonding, final part density, and the formation of defects such as porosity or lack of fusion. The goal was to analyze how these variations affect the corresponding mechanical behavior of AlSi10Mg, providing optimization criteria applicable to future functional applications. The energy density (VED) was calculated according to [Equation 1](#), which defines the relationship between the main SLM process parameters:

$$\text{VED} = \frac{P}{(v \cdot h \cdot t)} \quad (1)$$

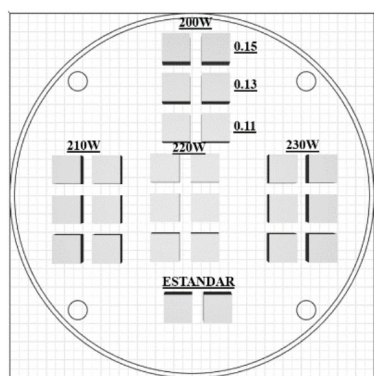
where P is the laser power (W), v is the scan speed (mm/s), h is the hatch distance (mm), and t is the layer thickness (mm) of the samples.

The resulting values are presented in [Table 2](#).

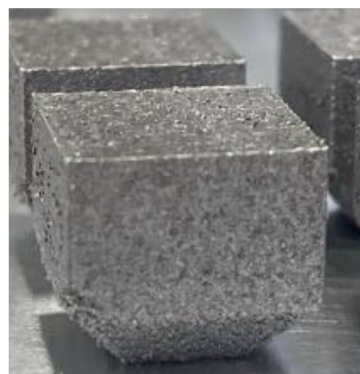
Table 1. Composition of the AlSi10Mg alloy employed in this work

Element	Si	Mg	Fe	Cu	Mn	Zn	Ti	Ni	Other (total)	Al
Weight %	10	0.3	≤ 0.55	≤ 0.05	≤ 0.45	≤ 0.10	≤ 0.15	≤ 0.05	≤ 0.15	$\sim 85\%$

Abbreviations: Al: Aluminum; Cu: Copper; Fe: Iron; Mg: Magnesium; Mn: Manganese; Ni: Nickel; Si: Silicon; Ti: Titanium; Zn: Zinc.



A



B

Figure 2. Truncated inverted pyramid samples produced for density, surface porosity, hardness, and microstructural characterization. (A) Schematic representation of the arrangement of specimens in the chamber along with studied laser powers and hatch spacings; (B) truncated inverted pyramid morphology of the produced samples.

Table 2. Process parameters for the fabrication of the specimens by selective laser melting

Specimen	Power (W)	Hatch distance (mm)	Energy density (J/mm ³)
1	200	0.11	91
2	200	0.13	77
3	200	0.15	67
4	210	0.11	95
5	210	0.13	81
6	210	0.15	70
7	220	0.11	100
8	220	0.13	85
9	220	0.15	73
10	230	0.11	105
11	230	0.13	88
12	230	0.15	77

The statistical analysis in this study was performed using two complementary approaches. First, a two-factor ANOVA was conducted to evaluate the significance of laser power and hatch spacing on each response variable, identifying which factors had a statistically significant effect. Second, a quadratic ordinary least squares regression model was fitted to the experimental data to describe the relationship between the response variables and the process parameters, including linear, quadratic, and interaction terms. The resulting regression surfaces were plotted together with the experimental points to assess the quality of the model fit visually. Standard model metrics, such as R^2 , adjusted R^2 , and F -statistics, are presented in accompanying tables to provide a quantitative evaluation of model performance. The conclusions drawn were limited to the investigated parameter range. Since laser power and hatch spacing jointly determine the effective energy input and melt pool behavior, their combined influence was also evaluated using the two-factor ANOVA (power \times hatch spacing) model, including interaction terms. Within the investigated parameter ranges, the interaction effect was found to be statistically insignificant, indicating that the main trends can be interpreted based on the dominant individual effects without strong coupling between parameters.

2.3. Characterization process

To ensure repeatability and improve the reliability of the measurements, all characterization tests were performed on three replicate specimens for each set of process parameters. The replicate measurements were used to assess experimental variability for the reported mechanical

and microstructural results.

2.3.1. Relative density

The apparent density of the parts was determined using the Archimedes method²⁰, by comparing the weight of each sample in air (W_{air}) and submerged in water (W_{water}). The density was calculated using the following expression:

$$\rho = \frac{W_{\text{air}}}{W_{\text{air}} - W_{\text{water}}} \cdot \rho_{\text{water}} \quad (2)$$

where ρ_{water} is the density of water. The samples were cleaned and dried prior to testing, and the measurements were carried out using a precision balance. The relative density was obtained by comparing the measured value with the theoretical density of AlSi10Mg (2.7 g/cm³), thus allowing an estimation of the internal porosity of each specimen.

The density of the specimens was measured using a Mettler Toledo analytical balance, model XS104 (Mettler-Toledo GmbH, Switzerland). This device has a maximum load capacity of 120 g and a readability of 0.1 mg, ensuring high precision in mass measurements required for accurate density evaluation.

2.3.2. Surface porosity

A custom Python-based image processing program (version 3.9.0, Python Software Foundation, USA) was developed to identify and quantify pores in the microscopy images of the samples. The script applies color filtering and grayscale thresholding techniques to distinguish the pore regions (dark areas) from the surrounding material while excluding non-relevant colored features. This automated approach ensures consistent and objective pore detection, providing a reliable estimation of porosity across the analyzed images. For each processing condition, three different surface regions were analyzed to ensure statistical representativeness and to reduce the influence of local heterogeneities. The reported porosity values correspond to the average of these measurements. This image-based methodology follows procedures commonly reported in the literature for porosity quantification in LPBF materials, where threshold-based segmentation is used to estimate surface pore fraction.^{21–23}

2.3.3. Hardness

Vickers hardness measurements were carried out using a Mitutoyo microhardness tester (Mitutoyo Corp., Kanagawa, Japan), equipped with a high-precision optical system for accurate indentation measurement under controlled loading conditions. A load of 10 N (HV1) was applied with a dwell time of 10 s. Prior to testing, the specimens were ground and polished to a mirror finish to eliminate

surface irregularities and oxides. The measurements were performed in accordance with ISO 6507-1 for Vickers hardness testing of metallic materials.

2.3.4. Impact energy

The Charpy impact test was performed to evaluate the fracture toughness and energy absorption capacity of the AlSi10Mg specimens under dynamic loading conditions. This test is particularly useful for identifying brittle behavior and assessing the influence of manufacturing defects, such as pores or lack of fusion, on the material's resistance to sudden fracture. The Charpy impact tests were performed using specimens prepared in accordance with ISO 148-1 (Figure 3A), ensuring standardized geometry and conditions for assessing the impact resistance of the material, with the samples having a cross-sectional area of 1 cm². The Charpy specimens were produced directly by SLM with the notch included. After fabrication, the Charpy notch was subjected to a surface finishing operation to improve its quality and dimensional accuracy. The notch geometry (radius and angle) was measured and verified to comply with ISO 148-1 tolerances.

Charpy impact energy was measured using a pendulum impact tester manufactured by Instron Wolpert, model

PW30 (USA). This equipment allows for the evaluation of fracture resistance under dynamic loading conditions, in accordance with standard impact testing procedures.

2.3.5. Tensile strength

Tensile tests were performed using a Tinius Olsen H25KS universal testing machine (Tinius Olsen Ltd., United Kingdom), equipped with a maximum load capacity of 25 kN and a force measurement accuracy of $\pm 0.5\%$. This system is designed for high-precision mechanical testing of metallic materials. The tensile tests were carried out using specimens prepared in accordance with ISO 6892-1 (Figure 3B), ensuring standardized geometry and testing conditions for reliable comparison of the mechanical properties obtained.

The equipment allows for a displacement range of up to 1,140 mm, with a crosshead speed range from 0.001 to 100 mm/s, enabling its use with a wide variety of specimen geometries and testing conditions. The column clearance is 400 mm, and the overall frame dimensions are 650 × 450 × 1,600 mm, with a total weight of 120 kg, ensuring mechanical stability during testing.

An integrated extension measurement system provides a resolution better than 0.01 μm , allowing for precise

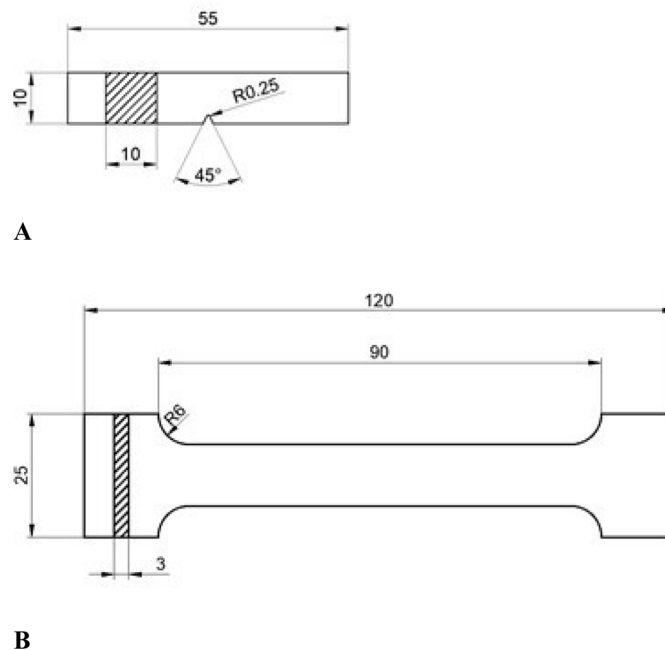


Figure 3. Specimen dimensions for Charpy and tensile strength characterization (A) Charpy specimen used in impact energy characterization of the samples following ISO 148-1; (B) specimen used for tensile characterization of the samples following ISO 6892-1.

strain monitoring throughout the test. These specifications make the H25KS particularly suitable for experimental studies requiring accurate characterization of mechanical properties.

2.3.6. Morphological characterization

Surface and fractography characterization were performed using field emission-scanning electron microscopy with a Hitachi S-3800 microscope (Hitachi Ltd., Japan). To reveal the microstructure on the surface of the SLM-fabricated AlSi10Mg specimens, a chemical etching process was carried out using a 10% NaOH aqueous solution. The specimens were immersed for 10–20 s at room temperature, followed by rinsing with distilled water and ethanol. This etchant selectively attacks the aluminum matrix, leaving the silicon-rich regions in relief, thereby enabling clear visualization of the microstructure under scanning electron microscopy.

4. Results

This section presents the characterization results and evaluates how the selected fabrication parameters influenced the SLM processing response of AlSi10Mg. To further analyze the influence results, a two-factor ANOVA was carried out to effectively evaluate the influence of the analyzed parameters on the studied samples, using Python-based statistical analysis.

4.1. Relative density

The relative density of the specimens was evaluated to assess the influence of laser power and hatch spacing on part consolidation. Figure 4 summarizes the relative-density values as a function of laser power and hatch

spacing.

Figure 4A shows the evolution of the relative density of AlSi10Mg specimens as a function of laser power in the SLM process. The results indicate that the highest densities are obtained at lower powers, specifically at 200 W and 210 W, where the relative density exceeds 99.8%. This trend can be attributed to the interplay between energy input and melt pool stability. At moderate laser powers, sufficient energy is delivered to ensure complete melting and effective interlayer fusion, resulting in minimal porosity and high densification. However, when the laser power increases to 220 W and above, the excessive energy input promotes unstable melt pool conditions, including keyhole formation, intensified vaporization, and spatter generation. These phenomena may favor pore formation and consequently reduce the relative density. The partial recovery observed at 230 W suggests a local stabilization of the melt pool under the selected processing conditions, although the results overall indicate that excessive energy input can negatively affect part consolidation.²⁴

Among the three tested hatch-spacing values, the highest density was obtained at a hatch spacing of 0.13 mm, reaching 99.75% (Figure 4B). In contrast, the lowest density corresponds to the 0.11 mm condition, with a value of 99.6%, followed closely by 0.15 mm at 99.65%. This trend may suggest that a hatch spacing of 0.13 mm provided a favorable balance between scan-track overlap and defect formation under the investigated conditions; however, hatch spacing did not significantly affect relative density within the tested range. An extremely small hatch spacing (0.11 mm) may lead to excessive remelting and local overheating, while a large spacing (0.15 mm) could result in incomplete melting between tracks, both of which

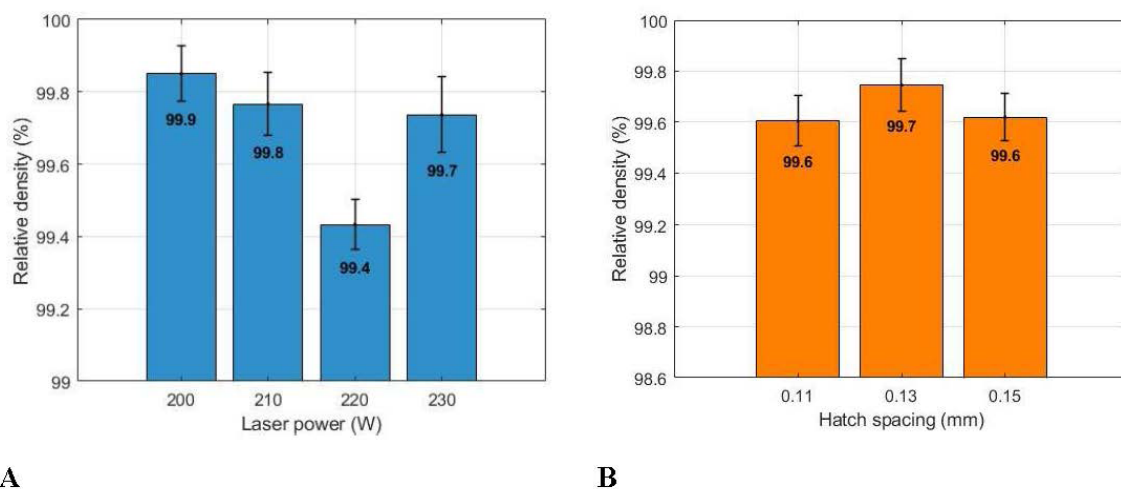


Figure 4. Relative density values for (A) studied laser powers and (B) studied hatch spacing

reduce part density. Lower density levels are typically associated with increased porosity, which negatively affects mechanical performance (especially tensile strength, fracture toughness, and fatigue resistance) by acting as stress concentrators and initiating premature failure under load.²⁵

The relative density values obtained in this study, almost all above 99.4% for the optimized processing window, are in line with those typically reported for AlSi10Mg components manufactured by SLM. Densities in the range of 99.3–99.8% are common in the literature when appropriate combinations of laser power, scanning speed, and hatch spacing are employed, ensuring sufficient energy input to fully melt the powder and minimize lack-of-fusion defects.^{20,26}

A two-factor ANOVA (laser power \times hatch spacing) conducted on the density values revealed a highly significant effect of laser power ($p = 0.003$), whereas hatch spacing did not show a statistically significant influence ($p = 0.3$) in the studied parameters. Although the F -value for hatch spacing (3) is slightly higher than that for power (1), significance is determined by the p -value, not the F -value alone. These results indicate that the density of SLM-fabricated parts decreases with increasing laser power, suggesting that higher energy input may promote greater melt pool turbulence or evaporation, slightly reducing material densification. In contrast, variations in hatch spacing within the studied range (0.11–0.15 mm) do not produce appreciable changes in density. The interaction effect between laser power and hatch spacing was also evaluated and did not show statistical significance ($p = 0.12$). This result indicates that no strong coupling between both parameters is present within the investigated range, and that the observed density trends are primarily governed by the main effect of laser power. The ANOVA analysis corresponding to the relative density parameters is shown in Table 3.

Table 3. Two-way ANOVA analysis for relative density parameters

Variation source	p -value	F -value
Power	0.003	1
Hatch spacing	0.3	3
Power \times hatch spacing	0.12	2

The regression surface for relative density, as shown in Figure 5, indicates that this parameter is largely independent of the hatch spacing, as the fitted surface shows minimal variation along this axis. In contrast, the relative density exhibits a clear dependence on laser power; the regression surface reveals a decreasing trend in density

with increasing power. Overall, the regression model captures the general pattern of the experimental data quite well. The measured points largely align with the fitted surface, confirming the validity of the model within the tested range. However, for the laser power of 230 W, some deviation is observed, with the experimental density values slightly exceeding the predictions. This suggests a minor nonlinearity or additional effects at high power levels that are not fully captured by the quadratic model.

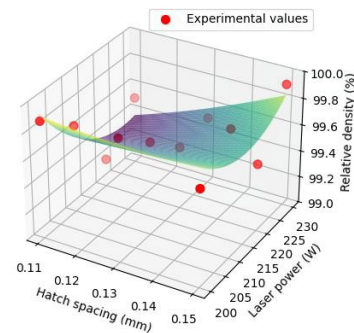


Figure 5. Regression surface of relative density as a function of laser power and hatch spacing

The summary of the regression model indicates that the model explains a substantial portion of the variability in relative density, with an R^2 of 0.6 and an adjusted R^2 of 0.4, suggesting a moderate fit after accounting for the number of predictors. The overall model is not statistically significant ($F = 2$, $p = 0.1$), indicating that the included predictors, collectively, have a meaningful effect on the response variable in the studied parameters. However, the very high condition number (2.6×10^8) points to potential multicollinearity among the predictors, likely due to the inclusion of quadratic and interaction terms, which should be considered when interpreting the individual coefficients. Overall, the model provides a reasonable approximation of the experimental data, particularly in capturing trends associated with laser power. The regression model of the relative density of samples is shown in Table 4.

Table 4. Summary of the ordinary least squares regression model for relative density

Metric	Value
R^2	0.6
Adjusted R^2	0.4
F -statistic	2
Prob (F -statistic)	0.1
Observations (n)	12
Condition number	2.6×10^8

Overall, both analyses corroborate that relative density is primarily controlled by laser power, and that variations in hatch spacing within the tested range have negligible impact.

4.2. Surface porosity

The formation of surface porosity in LPBF-processed AlSi10Mg is closely related to melt pool dynamics and energy density, which control defect formation mechanisms such as lack-of-fusion and keyholing. Understanding this relationship is essential to optimize mechanical performance and process stability.¹⁵ Figure 6 shows the surface-porosity values as a function of laser power and hatch spacing, displaying a clear inverse trend. Samples produced at 220 W exhibit the lowest relative density and the highest surface porosity, confirming the detrimental effect of excessive energy input on part consolidation. Notably, this condition also shows the largest standard deviation in porosity measurements, indicating increased variability and reduced process repeatability at this energy level. This scatter reflects unstable melt-pool behavior and may be associated with keyholing, vaporization, and spatter formation, which can lead to a non-uniform distribution of pores near the surface. In contrast, intermediate powers (200–210 W) yield the highest relative densities (>99.7%) and correspondingly lower porosity values (around 1–1.5%). The 230 W condition also maintains relatively low porosity, indicating partial recovery of stability at slightly higher powers. The overall high densification levels, with densities around 99.5% and surface porosities below 1.5%, demonstrate the effectiveness of the selected SLM parameters in minimizing lack-of-fusion defects. However, the localized increase in porosity at 220 W suggests that keyholing, vaporization, or unstable melt

pool dynamics may occur at this energy level, leading to trapped gas and pore formation near the surface.

Regarding the influence of hatch spacing on porosity, no clear trend is observed among the tested values in Figure 6b. The surface porosity remains relatively stable, ranging between 1.5% and 1.7% for hatch spacings of 0.11, 0.13, and 0.15 mm. These small variations fall within experimental uncertainty, indicating that hatch spacing does not have a significant effect on pore formation under the present processing conditions.

The surface porosity values obtained in this study, ranging between 1.1% and 2.8%, are consistent with those typically reported for SLM-fabricated AlSi10Mg alloys. In the literature, optimized processing conditions generally lead to surface porosity levels within 0.5–2.0%, depending on the measurement technique and image analysis method.^{27,28} It should be noted that surface porosity tends to be slightly higher than volumetric porosity, as it includes partially open or incomplete melt defects on the outer layers.¹³ The measured porosity values, together with relative densities above 99.5%, therefore indicate a high degree of material consolidation and proper fusion during the SLM process.

Figure 7A shows an example of the surface-porosity analysis for Specimen 9. In Figure 7B, the detected pores are highlighted in red by the image-processing routine. The program identifies and measures the pore fraction within the analyzed area.

A two-factor ANOVA conducted on the surface porosity values revealed that neither laser power ($p = 0.1$) nor hatch spacing ($p = 0.7$) exhibited a statistically significant effect within the investigated parameter range. Although the F -value for laser power (3) is higher than

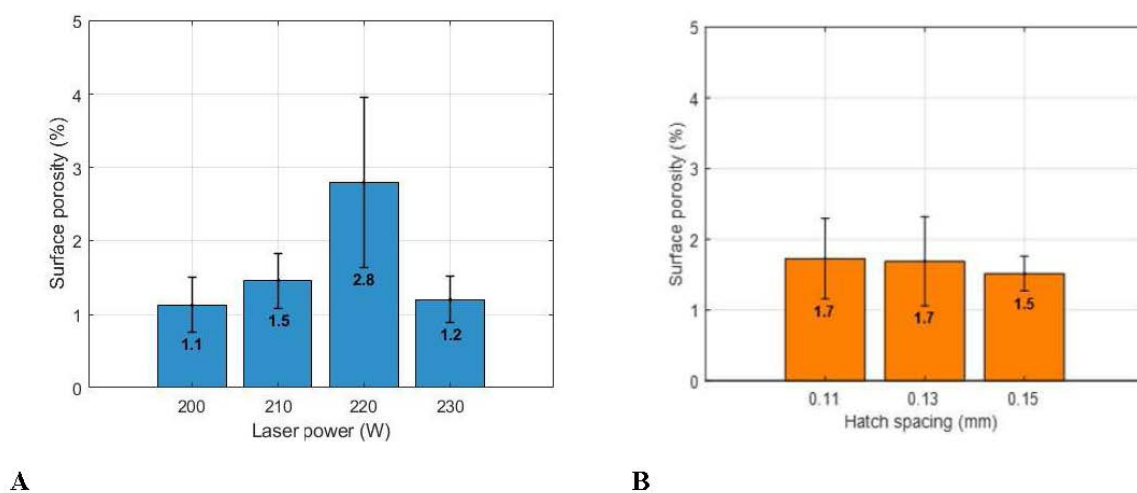


Figure 6. Porosity values for (A) studied laser powers and (B) studied hatch spacing

that for hatch spacing (0.1), statistical significance is determined by the p -value, which in both cases exceeds the conventional threshold of 0.05. These results suggest that surface porosity does not vary significantly with changes in laser power or hatch spacing within the studied intervals. This indicates that, under the selected processing conditions, surface porosity remains relatively stable and is not strongly governed by the moderate variations in energy input evaluated in this work. The interaction effect between laser power and hatch spacing was also analyzed and found to be statistically insignificant ($p = 0.6$), confirming the absence of a coupled influence of both parameters on surface porosity within the investigated range. Table 5 shows the ANOVA analysis values of the surface porosity parameter.

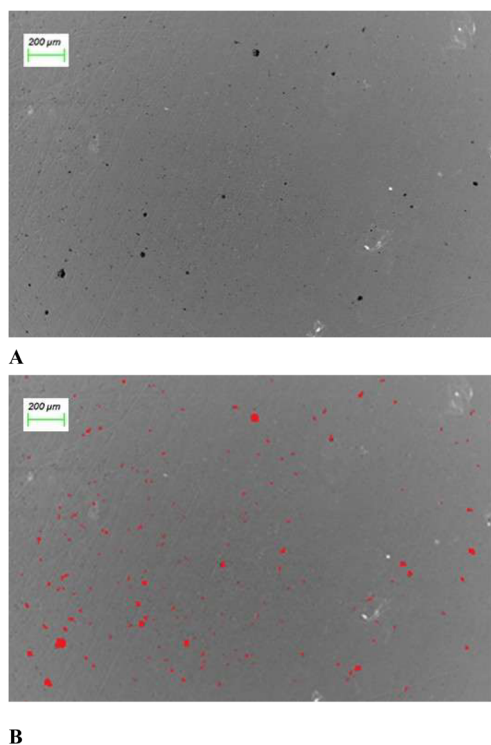


Figure 7. Surface porosity analysis of Specimen 9. (A) Surface morphology showing the presence of small spherical pores; (B) image processing routine developed in Python to quantify porosity. Scale bars: 200 µm; magnification: $\times 50$.

Table 5. Two-way ANOVA analysis for surface porosity parameter

Variation source	p -value	F -value
Power	0.1	3
Hatch spacing	0.7	0.1
Power \times hatch spacing	0.6	0.2

The regression surface for surface porosity shown in Figure 8 indicates that this parameter is largely independent of hatch spacing, as the fitted surface exhibits minimal variation along this axis within the studied range (0.11–0.15 mm). In contrast, porosity shows a slight dependence on laser power, with the regression surface suggesting higher porosity values at intermediate power levels. In particular, the specimens processed at 220 W exhibit comparatively higher porosity values; however, this condition is also associated with a larger standard deviation, indicating greater variability in the measurements.

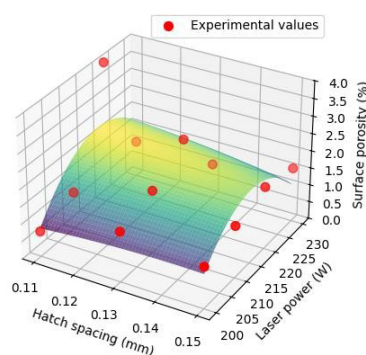


Figure 8. Regression surface of porosity as a function of laser power and hatch spacing

The summary of the regression model (Table 6) indicates that the model explains a limited portion of the variability in surface porosity, with an R^2 of 0.4 and an adjusted R^2 of -0.1 , suggesting a weak fit after accounting for the number of predictors. The overall model is not statistically significant ($F = 0.7$, $p = 0.6$), indicating that the included predictors, collectively, do not have a meaningful effect on the response variable within the studied parameter range.

Table 6. Summary of the ordinary least squares regression model for surface porosity

Metric	Value
R^2	0.4
Adjusted R^2	-0.1
F -statistic	0.7
Prob (F -statistic)	0.6
Observations (n)	12
Condition number	2.6×10^8

4.3. Hardness test

The measured Vickers hardness values show a clear dependency on the applied laser power during the SLM process (see Figure 9). As shown in Figure 9A, the

hardness remains relatively stable for samples produced at 200 W and 210 W, with average values around 124 HV. Notably, the sample produced at 210 W exhibits the largest standard deviation among all conditions, indicating higher variability in hardness measurements. This increased scatter may result from local microstructural heterogeneity or slight fluctuations in melt pool stability at this laser power. A significant drop in hardness is observed at 220 W, where the value decreases to approximately 117 HV. This reduction may be attributed to microstructural coarsening or insufficient melting uniformity at this intermediate power level. Interestingly, the highest hardness is achieved at 230 W, reaching nearly 140 HV. This suggests that higher energy input at this setting promotes a finer or more homogeneously distributed microstructure, potentially due to more complete melting and rapid solidification. Nevertheless, such improvements must be weighed against possible increases in residual stress or thermal distortion at higher powers.²⁹

The results shown in Figure 9B present a modest increase in hardness when the hatch spacing increases from 0.11 mm to 0.13 mm, rising from approximately 123 HV to 128 HV. A slight decrease is observed at 0.15 mm, though the hardness remains close to the maximum, suggesting a saturation effect. This trend may be explained by the balance between energy distribution and overlap between adjacent laser tracks. At 0.13 mm, the energy input appears sufficient to ensure proper fusion and homogeneity while avoiding excessive remelting or porosity. In contrast, the lower hardness at 0.11 mm could be related to higher heat accumulation or over-melting, which may coarsen the microstructure.¹⁵

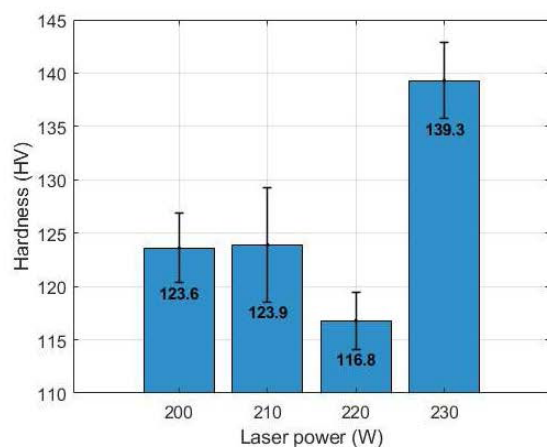
The two-factor ANOVA performed on the hardness

values revealed a significant effect of laser power ($p = 0.01$), whereas hatch spacing did not have a statistically significant influence ($p = 0.4$) within the analyzed parameter range. These results indicate that hardness is primarily affected by laser power, showing a marked increase at higher values (230 W), while variations in hatch spacing within the studied range (0.11–0.15 mm) do not produce appreciable changes. The interaction effect between laser power and hatch spacing was also evaluated and found to be statistically insignificant ($p = 0.6$), indicating that no coupled influence between both parameters affects hardness within the investigated range and confirming that the observed variation is mainly governed by the main effect of laser power. Table 7 shows the ANOVA analysis values of the hardness parameters.

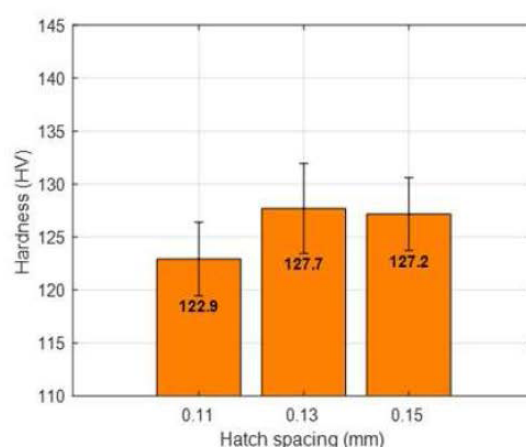
Table 7. Two-way ANOVA analysis for hardness parameters

Variation source	<i>p</i> -value	<i>F</i> -value
Power	0.01	4
Hatch spacing	0.4	5
Power × hatch spacing	0.6	2

The regression analysis of hardness (Figure 10) indicates that variations in hatch spacing have little to no effect, as evidenced by the almost flat surface along this axis. In contrast, increasing laser power results in a noticeable rise in hardness, demonstrating a clear positive correlation. The experimental data generally follow the predicted surface closely, confirming the model's accuracy. A minor discrepancy is observed at 220 W, where measured hardness values slightly exceed the regression predictions. Overall, the quadratic model provides a reliable representation



A



B

Figure 9. Vickers hardness (HV) values for (A) studied laser powers and (B) studied hatch spacing

of the dependence of hardness on laser power while highlighting areas where subtle deviations occur.

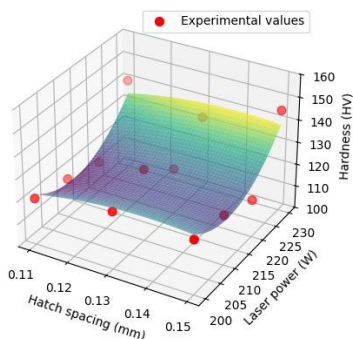


Figure 10. Regression surface of hardness value as a function of laser power and hatch spacing

The ordinary least squares regression model for hardness shows a moderate fit to the experimental data, with $R^2 = 0.64$, indicating that approximately 64% of the variability in hardness is explained by the model (Table 8). However, the adjusted R^2 is lower (0.3), reflecting the limited number of observations relative to the number of predictors. The overall model is not statistically significant ($F = 2$, $p = 0.2$), suggesting that the combined linear, quadratic, and interaction terms do not provide a strong predictive power for hardness in this studied dataset. Additionally, the high condition number (2.56×10^8) points to potential multicollinearity among predictors, likely due to the inclusion of quadratic and interaction terms.

Table 8. Summary of the ordinary least squares regression model for hardness

Metric	Value
R^2	0.6
Adjusted R^2	0.3
F -statistic	2
Prob (F -statistic)	0.2
Observations (n)	12
Condition number	2.6×10^8

The two-way ANOVA for hardness shows that laser power has a statistically significant effect, while hatch spacing does not. In comparison, the overall quadratic regression model does not reach statistical significance, likely due to the limited number of observations and the inclusion of quadratic and interaction terms. Despite this, the regression model captures the qualitative trend observed in the data: hardness increases with laser power and remains largely unaffected by hatch spacing.

The Vickers microhardness values obtained for the studied specimens range between approximately 120 and 140 HV, which are consistent with those typically reported for SLM-processed AlSi10Mg alloys. This hardness range reflects the fine cellular–dendritic microstructure formed during rapid solidification, characterized by a supersaturated α -Al matrix and a finely distributed Si network. The slight increase in hardness observed at higher laser powers (up to ~140 HV at 230 W) can be attributed to improved melting uniformity and reduced lack-of-fusion defects, although excessive energy input may also promote local coarsening or residual stress. Overall, the measured hardness values confirm the good consolidation and microstructural refinement achieved under the selected processing conditions.^{30,31}

4.4. Charpy characterization

Charpy impact tests were conducted to assess the toughness of AlSi10Mg specimens processed with different combinations of laser power and hatch spacing (see Tables 9 and 10, respectively).

Table 9. Impact energy for different laser power values

Laser power (W)	Impact energy (J)
200	10.5 ± 0.3
210	11.9 ± 0.6
220	10.7 ± 0.1
230	9.9 ± 0.5

This non-monotonic behavior suggests that an intermediate laser power may be more favorable for optimizing the energy absorption capacity of the material. Excessive or insufficient energy input can lead to microstructural heterogeneities or defect formation (porosity, lack of fusion), which reduce the material's ability to absorb impact without fracturing.

Table 10. Impact energy for different hatch spacing values

Hatch spacing (mm)	Impact energy (J)
0.11	10.6 ± 0.8
0.13	11.1 ± 0.9
0.15	10.9 ± 0.3

The differences among hatch-spacing conditions were small, and the ANOVA indicates that hatch spacing did not significantly affect impact energy within the investigated range. The decreased performance at 0.15 mm may be attributed to insufficient overlap between scan tracks,

which can reduce interlayer cohesion and facilitate brittle fracture under impact.³²

The ANOVA results indicate that laser power is again the dominant factor influencing Charpy impact toughness. In contrast, hatch spacing within the studied range (0.11–0.15 mm) does not produce appreciable changes in these properties. Therefore, variations in laser power have a significant effect on both hardness and impact toughness, while hatch spacing plays a negligible role under the tested conditions studied in this paper. The interaction effect between laser power and hatch spacing was also analyzed and found to be statistically insignificant ($p = 0.3$), indicating that no coupled influence between both parameters affects the impact toughness within the investigated range and confirming that the observed variations are mainly controlled by the main effect of laser power. Table 11 shows the ANOVA analysis values of samples toughness.

Table 11. Two-way ANOVA analysis for toughness parameter

Variation source	<i>p</i> -value	<i>F</i> -value
Power	0.02	4
Hatch spacing	0.4	5
Power \times hatch spacing	0.3	2

Figure 11 shows the regression surface for impact energy, which reveals that hatch spacing has negligible influence, as the surface remains essentially uniform along this axis. The laser power parameter exhibits a subtle effect: intermediate power levels correspond to slightly higher impact energy, while lower and higher powers produce reduced values. This trend is well captured by the regression model, and the experimental points align closely with the predicted surface, indicating that the model reliably represents the observed behavior. Overall, the analysis highlights that impact energy is primarily sensitive to moderate laser power levels, while remaining largely unaffected by variations in hatch spacing.

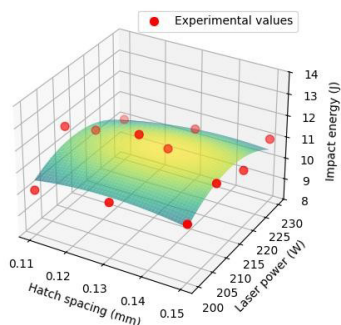


Figure 11. Regression surface of impact energy values as a function of laser power and hatch spacing

Table 12 shows the ordinary least squares regression model for impact energy, which presents a moderate R^2 value of 0.46, indicating that the model accounts for roughly 46% of the variability in the data. However, the adjusted R^2 is nearly zero (0.004), reflecting the limited predictive power of the model when considering the number of terms included. The overall model is not statistically significant ($F = 1$, $p = 0.2$) in the studied range of parameters. The very high condition number (2.6×10^8) indicates again potential multicollinearity among predictors, likely due to the inclusion of quadratic and interaction terms.

Table 12. Summary of the ordinary least squares regression model for impact energy

Metric	Value
R^2	0.4
Adjusted R^2	0.004
<i>F</i> -statistic	1
Prob (<i>F</i> -statistic)	0.2
Observations (<i>n</i>)	12
Condition number	2.6×10^8

According to the literature, Charpy impact-energy values for as-built AlSi10Mg typically lie within the range of approximately 8–12 J. For example, Kempen *et al.*¹³ reported impact toughness values for SLM parts comparable to cast material (~9–11 J). Another investigation, Girelli *et al.*³³ found slightly higher Charpy energy values in AM specimens versus cast analogues and underlined the importance of melt-pool quality. These relatively moderate toughness levels reflect the inherently brittle behavior of this alloy system, which is influenced by the presence of Si-rich phases and microstructural heterogeneities introduced during rapid solidification. The specimens processed at intermediate laser powers (around 210 W) exhibited slightly higher impact energies, suggesting that a balanced energy input improves layer cohesion and reduces stress concentration at pores or unmelted regions.

4.5. Tensile strength characterization

To evaluate the mechanical performance of AlSi10Mg parts fabricated by SLM, uniaxial tensile tests were carried out under standardized conditions. The main objective of this section is to analyze the influence of two key process parameters on the tensile response of the material, particularly on its ultimate tensile strength (UTS) and elongation at break. The tensile behavior of the specimens was assessed for selected combinations of laser power (200 W, 210 W, 220 W, and 230 W) and hatch spacing (0.11 mm,

0.13 mm, and 0.15 mm).

Among all tested conditions, as shown in Figure 12A, the configuration with 220 W yielded the highest UTS, reaching approximately 365 MPa with a hatch spacing of 0.15 mm. This value represents an improvement of approximately 3.8% compared to the second-best behavior corresponding to 210 W configuration (349 MPa), and 6.3% relative to the best result at 200 W (340 MPa). However, the UTS values do not show a clear monotonic dependence on laser power within the investigated range, as confirmed by the statistical analysis.

The elongation results do not show a clear or consistent dependence on either laser power or hatch spacing, which are shown in Figure 12B. The measured values fluctuate between approximately 1% and 4.5%, without a monotonic trend. Although slightly higher elongations are observed for some conditions (e.g., 200 W/0.13 mm and 210 W/0.11 mm), the overall variation suggests that other factors (such as local porosity distribution, microstructural inhomogeneities, or residual stresses) may play a more dominant role in determining ductility. The absence of a strong correlation indicates that elongation in SLM-processed AlSi10Mg is influenced by a complex interplay of process stability and defect formation rather than by the isolated effect of laser power or hatch spacing.³⁴

The optimal combination of 220 W laser power and 0.15 mm hatch spacing (Specimen 9) yielded a UTS of approximately 365 MPa. This result is in good agreement with previously reported values for SLM-processed AlSi10Mg. Kempen *et al.*¹³ reported tensile strengths close to 400 MPa using higher laser powers (350 W), while

Roth *et al.*¹⁴ achieved about 365 MPa under optimized conditions of 200 W and a narrower hatch spacing of 0.03 mm. Similarly, Gong *et al.*³⁵ obtained UTS values around 400 MPa with significantly higher power levels (around 500 W). The present results therefore demonstrate that comparable mechanical performance can be achieved at lower energy inputs, highlighting the efficiency and stability of the selected processing window.

In summary, the 220 W/0.15 mm configuration provided the most effective combination of parameters for tensile performance, likely due to an optimal balance between energy input, fusion quality, and microstructural consolidation. Although Specimen 9 (220 W, 0.15 mm) exhibits slightly lower relative density and hardness compared to the mean value of the samples, it shows superior tensile performance. This behavior does not fully align with the typical density–strength relationship reported in the literature.^{15,29} A possible explanation may lie in differences in pore morphology, size distribution, and defect type rather than total porosity alone. Thus, morphological and fractographic analyses were performed on this specimen.

The ANOVA analysis conducted on UTS values revealed that neither factor had a significant effect (power: $p = 0.2$; hatch spacing: $p = 0.2$). This indicates that, within the studied parameter range, neither laser power nor hatch spacing appreciably influences the tensile strength of the SLM-fabricated parts. The interaction effect between laser power and hatch spacing was also evaluated and found to be statistically insignificant ($p = 0.2$), indicating that no coupled influence of both parameters on tensile strength exists within the investigated range and confirming that

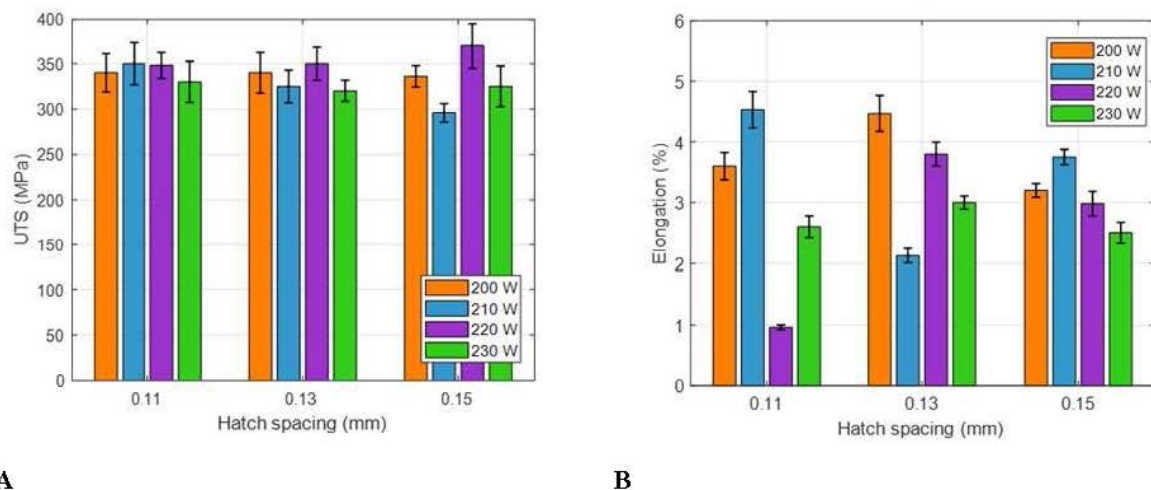


Figure 12. Tensile strength characterization results for the analyzed range of parameters. (A) Ultimate tensile strength (UTS) and (B) elongation obtained as a function of laser power (200, 210, 220, and 230 W) and hatch spacing (0.11, 0.13, and 0.15 mm). The values represent the mean of the tests with error bars corresponding to the standard deviation.

UTS remains relatively insensitive to moderate variations of these processing parameters. The ANOVA analysis values of the samples' tensile strength are shown in Table 13.

Table 13. Two-way ANOVA analysis for tensile strength parameter

Variation source	<i>p</i> -value	<i>F</i> -value
Power	0.2	0.6
Hatch spacing	0.2	0.6
Power \times hatch spacing	0.2	0.6

The regression surface for UTS indicates that, although variations in hatch spacing and laser power are present in Figure 13, these factors do not exert a significant influence on UTS, as also suggested by the ANOVA results. Consequently, the fitted regression model does not fully capture the experimental behavior, and several measured points deviate from the predicted surface. This suggests that UTS is largely independent of the tested process parameters, and that other factors not included in the current model may govern its variation. The results suggest the existence of a local optimum around 220 W, which may be associated with a favorable balance between densification, melt pool stability, and microstructural homogeneity rather than a dominant influence of increasing energy input.¹³

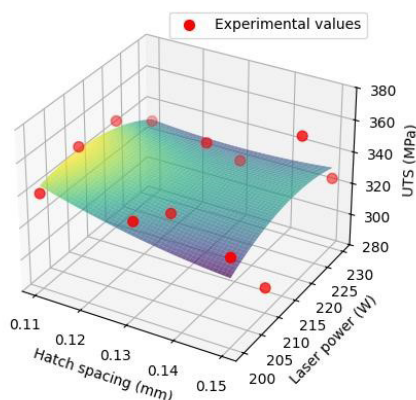


Figure 13. Regression surface of ultimate tensile strength (UTS) values as a function of laser power and hatch spacing

The regression analysis for UTS (Table 14) indicates that the fitted quadratic model explains around 10% of the variability in the experimental data ($R^2 = 0.1$). However, the adjusted R^2 is negative (-0.5), highlighting that the model has limited predictive capability when considering the number of predictors. Moreover, the overall model is not statistically significant ($F = 0.2$, $p = 0.9$), suggesting that the combination of linear, quadratic, and interaction terms

does not provide a reliable description of UTS variations in the analyzed parameter range.

Table 14. Summary of the ordinary least squares regression model for ultimate tensile strength

Metric	Value
R^2	0.1
Adjusted R^2	-0.5
<i>F</i> -statistic	0.2
Prob (<i>F</i> -statistic)	0.9
Observations (<i>n</i>)	12
Condition number	2.4×10^8

The two-way ANOVA agrees with the results of the quadratic regression model, which also fails to reach overall significance and shows limited predictive capability for the UTS parameter. Table 15 shows a comparison of the mechanical property values obtained in this work with those reported in literature.

Table 15. Comparison of present results with representative literature ranges for selective laser melting-processed AlSi10Mg

Parameter	Present work	Literature results	References
Density	>99.3%	99.0–99.8%	20,26,36,37
Hardness	120–140 HV	110–150 HV	30,31,38,39
Toughness	8–12 J	9–11 J	13,32,33,40
Ultimate tensile strength	300–365 MPa	300–400 MPa	13,14,34,35

4.6. Morphology analysis

The surface morphology of Specimen 9, which showed the highest UTS, is shown in Figure 14, revealing a very fine microstructure characterized by small aluminum-rich cells or dendrites decorated with a Si-rich network. The average cell size is approximately 0.6 μm . This ultrafine cellular structure is typical of AlSi10Mg alloys produced by SLM, where extremely high cooling rates promote the formation of a supersaturated Al matrix with a fine, non-equilibrium distribution of Si.²⁵ In addition, a limited number of small spherical pores are observed on the surface, likely associated with trapped gas or isolated lack-of-fusion defects. Specimen 9 shows a relative density value of 99.5 % and a porosity value of 1.8%. The relative density of this specimen was slightly below the mean value for the studied samples, whereas its porosity was slightly above the mean. However, these parameters are not markedly different from literature values and remain close to the mean values observed in the present work.^{13,15}

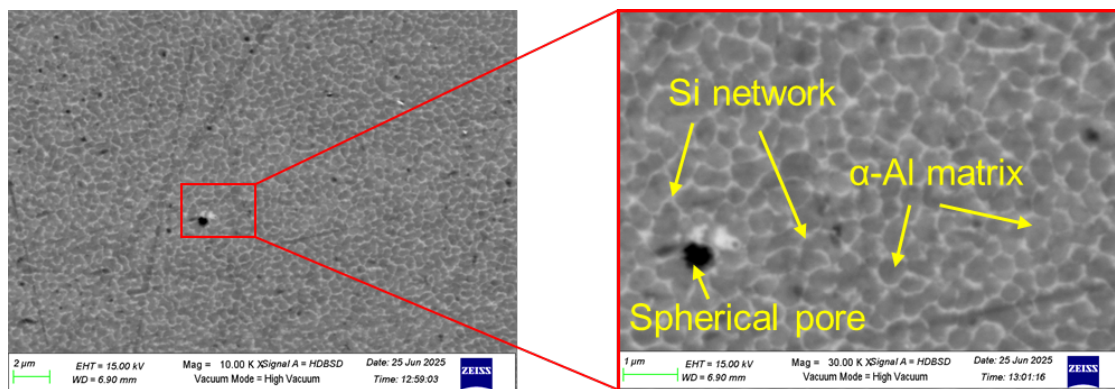


Figure 14. Surface scanning electron microscopic images of Specimen 9 showing the surface microstructure. Image at 10,000× magnification (left; scale bar: 2 μm) and image at 30,000× magnification (right; scale bar: 1 μm).

The observed microstructure, characterized by moderate porosity within the range of the studied specimens and a refined Si-decorated cellular network, correlates with the favorable mechanical performance of the specimen and highlights the influence of process parameters on microstructural control and part quality.

4.7. Fractography analysis

Figure 15A shows a general view of the fracture surface of Specimen 9, obtained using the HDBSD mode at 80× magnification. The image reveals a heterogeneous surface with a dominant grey region and localized darker (black) areas. The grey regions are typically associated with the aluminum matrix (AlSi10Mg), while the darker zones may correspond to Si-rich phases (Mg₂Si) or oxide inclusions, which appear darker in HDBSD mode due to differences in atomic number and signal intensity. The presence of Si-rich regions and oxide inclusions can significantly affect the mechanical performance of AlSi10Mg parts. Si-rich phases, while increasing hardness, may promote brittle fracture due to their inherent fragility, whereas oxide inclusions act as stress concentrators and potential crack initiation sites, reducing ductility and fracture toughness.²⁵

Figure 15B shows the fracture surface of Specimen 9 observed in secondary electron mode at 80× magnification. The image highlights a relatively flat and featureless surface, consistent with a brittle fracture mechanism. Unlike ductile fractures, which typically exhibit plastic deformation features such as dimples or microvoid coalescence, this surface lacks evidence of material necking or energy absorption prior to failure. The presence of sharp fracture facets and abrupt transitions between regions supports the interpretation of cleavage or intergranular fracture, characteristic of brittle behavior. These features indicate rapid crack propagation with minimal plasticity, possibly facilitated by the presence of hard silicon phases or oxide

inclusions acting as crack initiation points.^{14,41}

As shown in Figure 15C, spherical internal pores are clearly visible within the fracture surface of the specimen, while Figure 7A reveals the presence of surface pores in the same sample. As discussed in the results section, this specimen exhibited lower relative density values, slightly higher porosity values, and lower hardness values compared with the mean results of the compared samples' parameters. However, these values do not deviate markedly from the mean values obtained in other samples nor from samples obtained in literature.^{13–15} This improvement in tensile performance cannot be attributed to a finer grain or cellular distribution, since such refinement would typically also increase hardness. Therefore, the enhanced tensile behavior is likely associated with a more favorable solidification pattern and improved interlayer bonding promoted by the specific combination of laser power and hatch spacing, which together optimize microstructural cohesion and load transfer efficiency despite the presence of pores.¹³

Figure 15D presents a higher-magnification image (5,000×) of the fracture surface of Specimen 9, acquired in secondary electron mode. This micrograph reveals more detailed features of the failure surface, showing fine lamellar structures. These features are likely associated with the fragmentation of the eutectic Al–Si phase, formed during rapid solidification. The lamellar morphology, coupled with the presence of spherical pores, further confirms the brittle fracture behavior and highlights the influence of microstructural heterogeneities resulting from the AM process.¹³

An energy-dispersive X-ray spectroscopy analysis was performed on the fracture surface of Specimen 9 to assess its local chemical composition (Figure 16). The results revealed the presence of the principal alloying elements

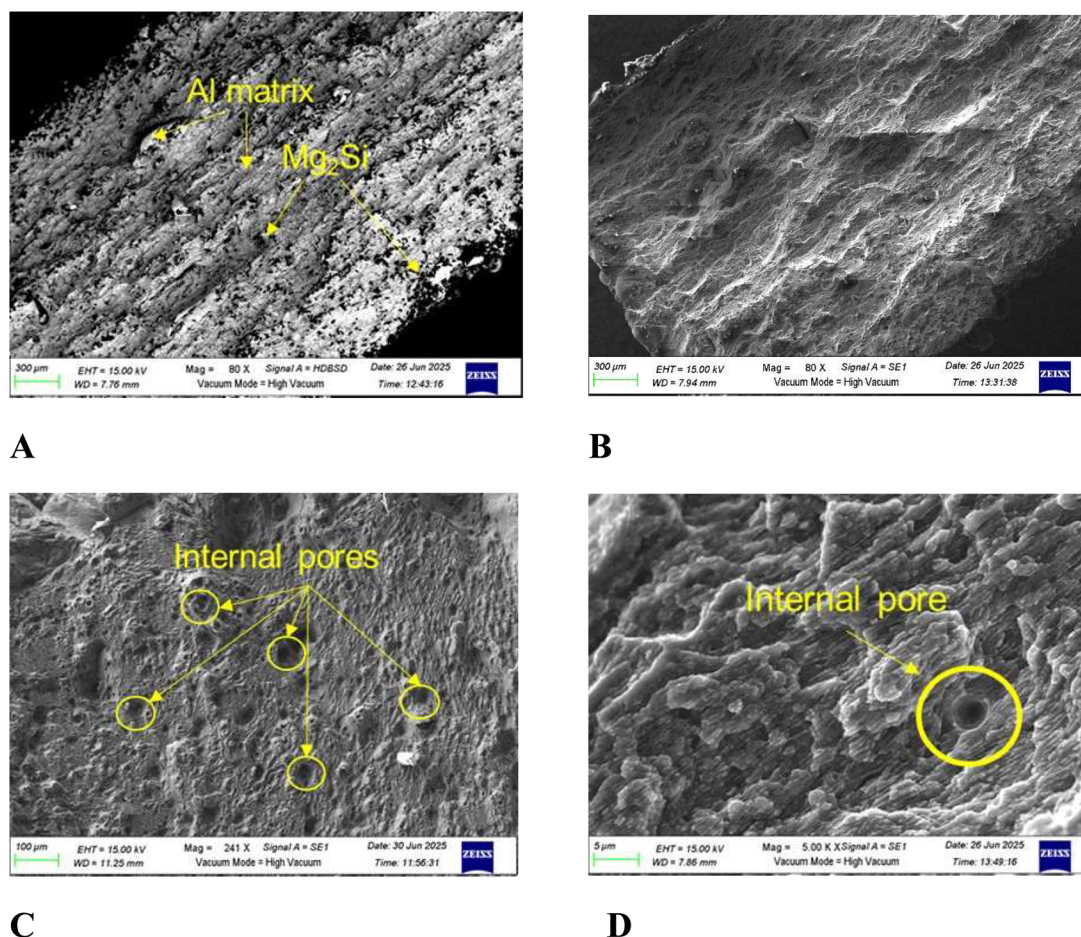


Figure 15. Fractography of Specimen 9 obtained via field emission scanning electron microscopy. (A) Image acquired in HDBSD mode at 80× magnification (scale bar: 300 μm). (B) Image acquired in secondary electron (SE) mode at 80× magnification (scale bar: 300 μm). (C) SE mode image at 200× magnification (scale bar: 100 μm). (D) SE mode image at 5,000× magnification (scale bar: 5 μm).

in Table 16, with measured values of 90.2 wt.% Al, 8.4 wt.% Si, and 1.3 wt.% Mg. This composition is consistent with the nominal chemistry of AlSi10Mg alloys processed by LPBF. The detected Si content supports the presence of Si-enriched regions typically observed as a cellular or network-like structure in additively manufactured AlSi10Mg. Mg was detected at lower concentration, which is consistent with the possible presence of Mg-containing phases reported in similar systems.^{42,43}

Table 16. Element composition (wt.%) of the analyzed area in Specimen 9

Element	Weight (%)
Mg	1.3
Al	90.2
Si	8.4

Abbreviations: Al: Aluminum; Mg: Magnesium; Si: Silicon.

In general, the combination of lamellar structure, brittle morphology, and porosity supports the conclusion that the fracture was influenced both by intrinsic material characteristics (silicon-rich phases) and process-related defects (pores, lack of fusion). In certain areas, small, rounded depressions (indicative of dimples) can be observed, suggesting a limited degree of localized plastic deformation. The coexistence of these features indicates a mixed fracture mode, where brittle cleavage dominates, but some ductile behavior is present at the microscale. The absence (or limited presence) of microcracks suggests that extensive intergranular cracking was not the dominant fracture mode in the imaged area, but rather along weaker zones associated with Si-rich phases or small process-induced defects. Overall, this morphology is consistent with the brittle-to-semi-ductile fracture behavior commonly reported for SLM-processed AlSi10Mg alloys, where rapid solidification and fine microstructure restrict extensive plastic deformation before failure.^{13,14}

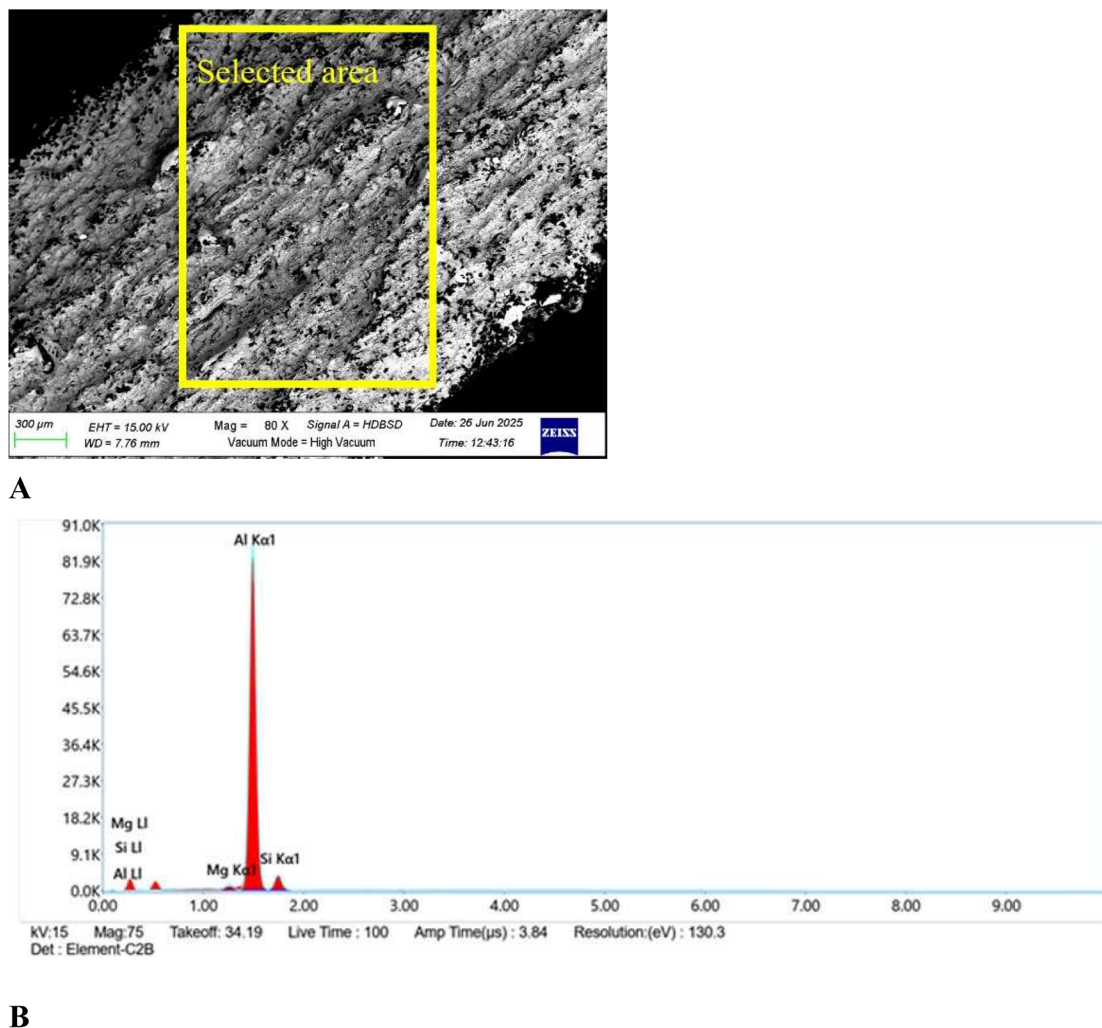


Figure 16. Energy-dispersive X-ray spectroscopy analysis of the fracture area in Specimen 9. (A) Analysed area of Specimen 9. Scale bars: 300 μm; magnification: 80×. (B) Composition profile of the analyzed area.

5. Conclusion

This study systematically examined the combined influence of laser power and hatch spacing on the density, mechanical properties, and microstructural characteristics of AlSi10Mg specimens fabricated via SLM. By varying these two key process parameters within controlled experimental conditions, this work provides a comprehensive understanding of how energy input and scan strategy interact to affect part consolidation, hardness, impact toughness, and tensile performance. The novelty of this work lies in the systematic and statistically supported evaluation of the combined effects of laser power and hatch spacing on the mechanical performance and microstructural integrity of SLM-processed AlSi10Mg,

demonstrating that optimal tensile behavior does not necessarily coincide with maximum density or hardness. The main findings can be summarized as follows:

- Laser power is the dominant process parameter controlling densification performance in SLM AlSi10Mg, while hatch spacing shows a secondary and statistically insignificant influence within the investigated range. The highest relative densities (>99.7%) and lowest surface porosities were achieved at low laser powers (200–210 W), whereas higher powers promoted porosity due to keyholing, vaporization, and melt pool instability.
- Hardness increased with increasing laser power, reaching approximately 140 HV at 230 W, although

regression analysis indicates that laser power is not globally significant when the studied parameters are considered simultaneously.

- Impact behavior was influenced by laser power, with maximum Charpy impact energy obtained at 210 W, suggesting an optimal balance between energy input and hatch spacing.
- The highest UTS was achieved at 220 W with a hatch spacing of 0.15 mm, despite slightly lower density and hardness, demonstrating that tensile performance is governed not only by densification but also by solidification patterns, microstructural homogeneity, and defect distribution.
- The two-factor ANOVA performed for all response variables showed that the interaction between laser power and hatch spacing was not statistically significant, indicating that no strong coupling exists between these parameters and confirming that their effects can be interpreted independently within the investigated processing range.
- Microstructural and fractographic analyses revealed an Al cellular network decorated with Si and predominantly brittle fracture behavior, with failure influenced by Si-rich phases and process-induced spherical porosity.

Interestingly, despite its slightly lower relative density and hardness, the specimen processed at 220 W with a hatch spacing of 0.15 mm exhibited the best tensile performance, suggesting that an optimal solidification pattern and interlayer bonding can compensate for moderate porosity levels. These insights contribute to a better understanding of process–property relationships and support the optimization of SLM parameters for high-quality, reliable aluminum alloy components. Although this study focused on relatively low SLM parameter values, the observed trends provide generalizable insights that can guide parameter selection, defect control, and process optimization in future AM applications with advanced machines.

Future work should extend the present methodology to wider parameter ranges, different build orientations, and more complex geometries. Further research may also focus on coupling process parameter optimization with tailored post-processing treatments to enhance ductility and fatigue performance, thereby supporting the reliable industrial implementation of SLM-fabricated AlSi10Mg components.

Acknowledgments

The authors would like to express their gratitude to Pablo Pujol from UCTAI (Unidad Científico-Técnica de Apoyo a la Investigación) for his support in the SEM analysis.

Funding

This research was funded by the Spanish Ministry of Science and Innovation (MCIN/AEI/10.13039/501100011033) under the project FactorIA (grant number: PLEC2024-011165) and supported as part of the MMAM project by the Euroregion Nouvelle-Aquitaine Euskadi Navarra through the “Euroregional Innovation” program.

Conflict of interest

Fernando Veiga serves as the Editorial Board Member of the journal, but did not in any way involve in the editorial and peer-review process conducted for this paper, directly or indirectly. Other authors declare they have no competing interests.

Author contributions

Conceptualization: Xabier Sandua, Eneko Arbizu, Fernando Veiga, Pedro J. Rivero

Formal analysis: Xabier Sandua, Miguel Ángel Martín

Funding acquisition: Fernando Veiga

Investigation: Xabier Sandua, Eneko Arbizu, Álvaro Rodríguez, Fernando Veiga,

Miguel Ángel Martín

Methodology: Xabier Sandua, Fernando Veiga, Miguel Ángel Martín

Supervision: Fernando Veiga

Writing—original draft: Xabier Sandua, Eneko Arbizu

Writing—review & editing: Álvaro Rodríguez, Fernando Veiga, Pedro J. Rivero

Ethics approval and consent to participate

Not applicable.

Consent for publication

Not applicable.

Availability of data

The data will be made available upon request.

References

1. Klenam DEP, McBagonluri F, Asumadu TK, Osei ED, Mornah D, Soboyejo WO. Additive manufacturing: shaping the future of the manufacturing industry – overview of trends, challenges and opportunities. *Appl Eng Sci.* 2025;22:100224.
doi: 10.1016/j.apples.2025.100224
2. Mohanavel V, Ashraff Ali KS, Ranganathan K, Allen Jeffrey J, Ravikumar MM, Rajkumar S. The roles and applications of additive manufacturing in the aerospace and automobile sector. *Mater Today Proc.* 2021;47:405-409.

- doi: 10.1016/j.matpr.2021.04.596
3. Chowdhury S, Yadaiah N, Prakash C, Dixit S, Gupta LR, Buddhi D. Laser powder bed fusion: a state-of-the-art review of the technology, materials, properties & defects, and numerical modelling. *J Mater Res Technol.* 2022;20:2109-2172.
doi: 10.1016/j.jmrt.2022.07.121
4. Spears TG, Gold SA. In-process sensing in selective laser melting (SLM) additive manufacturing. *Integr Mater Manuf Innov.* 2016;5(1):16-40.
doi: 10.1186/s40192-016-0045-4
5. Dejene ND, Lemu HG. Current Status and Challenges of Powder Bed Fusion-Based Metal Additive Manufacturing: Literature Review. *Metals.* 2023;13(2):424.
doi: 10.3390/met13020424
6. Majeed A, Lv J, Zhang Y, Shamim K, Qureshi ME, Zafar F. An investigation into the influence of processing parameters on the surface quality of AlSi10Mg parts by SLM process. In: 2019 16th International Bhurban Conference on Applied Sciences and Technology (IBCAST). IEEE; 2019:143-147.
doi: 10.1109/ibcast.2019.8667175
7. Trevisan F, Calignano F, Lorusso M, Lombardi M, Fino P, Manfredi D. On the Selective Laser Melting (SLM) of the AlSi10Mg Alloy: Process, Microstructure, and Mechanical Properties. *Materials.* 2017;10(1):76.
doi: 10.3390/ma10010076
8. Romano S. Quality control of AlSi10Mg produced by SLM_ Metallography versus CT scans for critical defect size assessment. *Addit Manuf.* 2019;28:394-405.
doi: 10.1016/j.addma.2019.05.017
9. Praneeth J, Venkatesh S, Sivarama Krishna L. Process parameters influence on mechanical properties of AlSi10Mg by SLM. *Mater Today Proc.* 2023.
doi: 10.1016/j.matpr.2022.12.222
10. Campanelli SL, Contuzzi N, Posa P, Angelastro A. Printability and Microstructure of Selective Laser Melting of WC/Co/Cr Powder. *Materials.* 2019;12(15):2397.
doi: 10.3390/ma12152397
11. Tolosa I, Garciandía F, Zubiri F, Zapiain F, Esnaola A. Study of mechanical properties of AISI 316 stainless steel processed by “selective laser melting”, following different manufacturing strategies. *Int J Adv Manuf Technol.* 2010;51(5-8):639-647.
doi: 10.1007/s00170-010-2631-5
12. Maamoun AH, Xue YE, Elbestawi MA, Veldhuis SC. The Effect of Selective Laser Melting Process Parameters on the Microstructure and Mechanical Properties of Al6061 and AlSi10Mg Alloys. *Materials.* 2018;12(1):12.
doi: 10.3390/ma12010012
13. Kempen K. Mechanical Properties of AlSi10Mg Produced by Selective Laser Melting. *Phys Procedia.* 2012;39:439-446.
doi: 10.1016/j.phpro.2012.10.059
14. Roth CC, Tancogne-Dejean T, Mohr D. Plasticity and fracture of cast and SLM AlSi10Mg: High-throughput testing and modeling. *Addit Manuf.* 2021;43:101998.
doi: 10.1016/j.addma.2021.101998
15. Snopiński P, Woźniak A, Pagáč M. Microstructural Evolution, Hardness, and Strengthening Mechanisms in SLM AlSi10Mg Alloy Subjected to Equal-Channel Angular Pressing (ECAP). *Materials.* 2021;14(24):7598.
doi: 10.3390/ma14247598
16. Read N, Wang W, Essa K, Attallah MM. Selective laser melting of AlSi10Mg alloy: Process optimisation and mechanical properties development. *Mater Des.* 2015;65:417-424.
doi: 10.1016/j.matdes.2014.09.044
17. Maamoun AH, Elbestawi M, Dosbaeva GK, Veldhuis SC. Thermal post-processing of AlSi10Mg parts produced by Selective Laser Melting using recycled powder. *Addit Manuf.* 2018;21:234-247.
doi: 10.1016/j.addma.2018.03.014
18. Aboulkhair NT, Simonelli M, Parry L, Ashcroft I, Tuck C, Hague R. 3D printing of Aluminium alloys: Additive Manufacturing of Aluminium alloys using selective laser melting. *Prog Mater Sci.* 2019;106:100578.
doi: 10.1016/j.pmatsci.2019.100578
19. GmbH MMS. m4p material solutions|metals for printing. Published online 2023. Available from: <https://www.metals4printing.com> [Last accessed on February 28, 2026]
20. Chen Z, Wei Z, Wei P, et al. Experimental Research on Selective Laser Melting AlSi10Mg Alloys: Process, Densification and Performance. *J Mater Eng Perform.* 2017;26(12):5897-5905.
doi: 10.1007/s11665-017-3044-5
21. Chawla K, Talabi SI, Rodriguez B, et al. Benchmarking image processing techniques for porosity measurement in polymer additive manufacturing: Review and experimental analysis. *Compos Part B Eng.* 2025;307:112857.
doi: 10.1016/j.compositesb.2025.112857
22. Pyka G, Kerckhofs G, Schrooten J, Wevers M. The effect of spatial micro-CT image resolution and surface complexity on the morphological 3D analysis of open porous structures. *Mater Charact.* 2014;87:104-115.
doi: 10.1016/j.matchar.2013.11.004
23. Cai X, Malcolm AA, Wong BS, Fan Z. Measurement and characterization of porosity in aluminium selective laser melting parts using X-ray CT. *Virtual Phys Prototyp.*

- 2015;10(4):195-206.
doi: 10.1080/17452759.2015.1112412
24. Ghio E, Cerri E. Work Hardening of Heat-Treated AlSi10Mg Alloy Manufactured by Selective Laser Melting: Effects of Layer Thickness and Hatch Spacing. *Materials*. 2021;14(17):4901.
doi: 10.3390/ma14174901
25. Li X, Liu Y, Tan C, Zou Y. Porosity formation mechanisms, microstructure evolution and mechanical performance of AlMgScZr alloy fabricated by laser powder bed fusion: Effect of hatch distance. *J Manuf Process*. 2023;94:107-119.
doi: 10.1016/j.jmapro.2023.03.047
26. Arvieu C, Galy C, Le Guen E, Lacoste E. Relative Density of SLM-Produced Aluminum Alloy Parts: Interpretation of Results. *JMMP*. 2020;4(3):83.
doi: 10.3390/jmmp4030083
27. Weingarten C, Buchbinder D, Pirch N, Meiners W, Wissenbach K, Poprawe R. Formation and reduction of hydrogen porosity during selective laser melting of AlSi10Mg. *J Mater Process Technol*. 2015;221:112-120.
doi: 10.1016/j.jmatprotec.2015.02.013
28. Aboulkhair NT, Everitt NM, Ashcroft I, Tuck C. Reducing porosity in AlSi10Mg parts processed by selective laser melting. *Addit Manuf*. 2014;1-4:77-86.
doi: 10.1016/j.addma.2014.08.001
29. Zhou L, Mehta A, Schulz E, McWilliams B, Cho K, Sohn Y. Microstructure, precipitates and hardness of selectively laser melted AlSi10Mg alloy before and after heat treatment. *Mater Charact*. 2018;143:5-17.
doi: 10.1016/j.matchar.2018.04.022
30. Měšiček J, Čegan T, Ma QP, *et al*. Effect of artificial aging on the strength, hardness, and residual stress of SLM AlSi10Mg parts prepared from the recycled powder. *Mater Sci Eng A*. 2022;855:143900.
doi: 10.1016/j.msea.2022.143900
31. Wang L zhi, Wang S, Hong X. Pulsed SLM-manufactured AlSi10Mg alloy: Mechanical properties and microstructural effects of designed laser energy densities. *J Manuf Process*. 2018;35:492-499.
doi: 10.1016/j.jmapro.2018.09.007
32. Yasa E, Deckers J, Kruth JP, Rombouts M, Luyten J. Charpy impact testing of metallic selective laser melting parts. *Virtual Phys Prototyp*. 2010;5(2):89-98.
doi: 10.1080/17452751003703894
33. Girelli L, Giovagnoli M, Tocci M, *et al*. Evaluation of the impact behaviour of AlSi10Mg alloy produced using laser additive manufacturing. *Mater Sci Eng A*. 2019;748:38-51.
doi: 10.1016/j.msea.2019.01.078
34. Maconachie T, Leary M, Zhang J, Lu G, Faruque O, Brandt M. Effect of build orientation on the quasi-static and dynamic response of SLM AlSi10Mg. *Mater Sci Eng A*. 2020;788:139445.
doi: 10.1016/j.msea.2020.139445
35. Gong J, Wei K, Liu M, Song W, Li X, Zeng X. Microstructure and mechanical properties of AlSi10Mg alloy built by laser powder bed fusion/direct energy deposition hybrid laser additive manufacturing. *Addit Manuf*. 2022;59:103160.
doi: 10.1016/j.addma.2022.103160
36. Bai S, Perevoshchikova N, Sha Y, Wu X. The Effects of Selective Laser Melting Process Parameters on Relative Density of the AlSi10Mg Parts and Suitable Procedures of the Archimedes Method. *Appl Sci*. 2019;9(3):583.
doi: 10.3390/app9030583
37. Majeed A, Zhang Y, Lv J, Peng T, Atta Z, Ahmed A. Investigation of T4 and T6 heat treatment influences on relative density and porosity of AlSi10Mg alloy components manufactured by SLM. *Comput Ind Eng*. 2020;139:106194.
doi: 10.1016/j.cie.2019.106194
38. Serjouei A, Libura T, Brodecki A, *et al*. Strength-hardness relationship for AlSi10Mg alloy produced by laser powder bed fusion: An experimental study. *Mater Sci Eng A*. 2022;861:144345.
doi: 10.1016/j.msea.2022.144345
39. Gao C, Wu W, Shi J, Xiao Z, Akbarzadeh AH. Simultaneous enhancement of strength, ductility, and hardness of TiN/AlSi10Mg nanocomposites via selective laser melting. *Addit Manuf*. 2020;34:101378.
doi: 10.1016/j.addma.2020.101378
40. Rosenthal I, Shneck R, Stern A. Heat treatment effect on the mechanical properties and fracture mechanism in AlSi10Mg fabricated by additive manufacturing selective laser melting process. *Mater Sci Eng A*. 2018;729:310-322.
doi: 10.1016/j.msea.2018.05.074
41. Tradowsky U, White J, Ward RM, Read N, Reimers W, Attallah MM. Selective laser melting of AlSi10Mg: Influence of post-processing on the microstructural and tensile properties development. *Mater Des*. 2016;105:212-222.
doi: 10.1016/j.matdes.2016.05.066
42. Larrosa NO, Wang W, Read N, *et al*. Linking microstructure and processing defects to mechanical properties of selectively laser melted AlSi10Mg alloy. *Theor Appl Fract Mech*. 2018;98:123-133.
doi: 10.1016/j.tafmec.2018.09.011
43. Patakhham U, Palasay A, Wila P, Tongsri R. MPB characteristics and Si morphologies on mechanical

properties and fracture behavior of SLM AlSi10Mg. *Mater
Sci Eng A*. 2021;821:141602.

doi: 10.1016/j.msea.2021.141602